# Two-Stage Random Alternation Framework for Zero-Shot Pansharpening

Haorui Chen\* Zeyu Ren\* Jiaxuan Ren Ran Ran Jinliang Shao Jie Huang Liangjian Deng † University of Electronic Science and Technology of China

{hrchen, zeyuren, jiaxuan.ren, ranran}@std.uestc.edu.cn, liangjian.deng@uestc.edu.cn

## **Abstract**

In recent years, pansharpening has seen rapid advancements with deep learning methods, which have demonstrated impressive fusion quality. However, the challenge of acquiring real high-resolution images limits the practical applicability of these methods. To address this, we propose a twostage random alternating framework (TRA-PAN) that effectively integrates strong supervision constraints from reducedresolution images with the physical characteristics of fullresolution images. The first stage introduces a pre-training procedure, which includes Degradation-Aware Modeling (DAM) to capture spatial-spectral degradation mappings, alongside a warm-up procedure designed to reduce training time and mitigate the negative effects of reduced-resolution data. In the second stage, Random Alternation Optimization (RAO) is employed, where random alternating training leverages the strengths of both reduced- and full-resolution images, further optimizing the fusion model. By primarily relying on full-resolution images, our method enables zeroshot training with just a single image pair, obviating the need for large datasets. Experimental results demonstrate that TRA-PAN outperforms state-of-the-art (SOTA) methods in both quantitative metrics and visual quality in real-world scenarios, highlighting its strong practical applicability.

## 1. Introduction

In remote sensing, high-resolution imagery is crucial for many applications [23, 42, 45]. However, due to satellite sensor limitations, multispectral and panchromatic images are usually captured separately [13]. Low-resolution multispectral (LRMS) images are used for spectral information, while high-resolution panchromatic (PAN) images provide spatial detail. The challenge is to effectively combine these images into a high-resolution multispectral (HRMS) image. This process, known as pansharpening, has proven to be an

effective tool for achieving this goal.

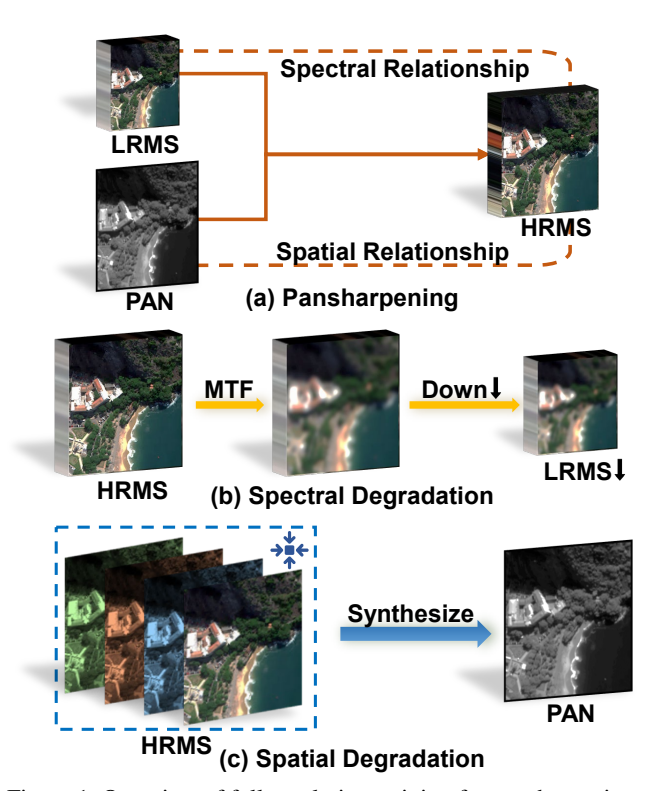


Figure 1. Overview of full-resolution training for pansharpening. (a) The pansharpening process highlights spectral and spatial relationships, linking LRMS and PAN images with the HRMS image. (b) The spectral degradation from HRMS to LRMS, including MTF and downsampling. (c) By synthesizing the channels in HRMS, such as the RGB channels shown in the figure, the spatial relationship between HRMS and PAN is learned.

Pansharpening techniques have evolved from traditional methods to deep learning (DL) approaches [4, 19, 26, 40, 41, 43]. Traditional methods like component substitution (CS) [5, 32], multi-resolution analysis (MRA) [33, 35], and variational optimization (VO) [11, 12, 29] rely on a solid mathematical foundation to merge spatial and spectral information without requiring large training datasets. However, these methods often face issues such as spectral distortion

<sup>\*</sup>Equal contribution.

<sup>&</sup>lt;sup>†</sup>Corresponding author.

and spatial misalignment. In contrast, DL-based techniques, supported by advances in hardware and software, offer improved preservation of both spectral and spatial features in high-resolution images.

However, DL-based methods require large amounts of data for training, but real high-resolution images are often difficult to obtain due to sensor limitations. This lack of real ground-truth supervision results in unsatisfactory fusion in real-world scenarios, limiting their application. To address this challenge, the most straightforward method is to perform unsupervised training on full-resolution images. This method models the spatial degradation from HRMS to PAN and the spectral degradation from HRMS to LRMS, as shown in Fig. 1 (a). By constraining spectral consistency between HRMS and LRMS and aligning spatial details with the PAN image, the model can be trained without explicit labels. To simulate spectral degradation, HRMS is first filtered with modulation transfer function (MTF) filters based on the sensor's optical properties. It is then downsampled and paired with LRMS, as shown in Fig. 1 (b). The spatial relationship between HRMS and PAN is modeled through methods such as linear degradation [17, 39], as shown in Fig. 1 (c). By modeling both spectral and spatial relationships, this fullresolution training method is obtained, as shown in Fig. 2 (a). However, oversimplifying the imaging process often causes the spectral response of the reconstructed image to deviate from the real data.

To overcome distortions caused by inaccurate manual modeling in full-resolution training, simulation methods similar to those used in full-resolution training can be applied to construct a synthetic dataset for supervised training. High-resolution images can be filtered using MTF and then downsampled to create synthetic training sets, learning the mapping from LRMS/PAN to HRMS. This end-to-end training at reduced-resolution allows the model to learn complex relationships between PAN, LRMS, and HRMS, as shown in Fig. 2 (b). Although this method uses pixel-level supervision, its performance is limited by the distribution discrepancy between simulated data and real images. Additionally, these methods rely on a "scale-invariance" assumption, which expects networks trained at reduced-resolution will perform equally well at full-resolution, but this assumption is not always valid [6]. In general, both reduced- and full-resolution training have their limitations. A potential solution [3, 30, 42] is multi-scale training, as shown in Fig. 2 (c), but this approach often treats the two resolutions separately, leading to a lack of information transfer and fusion. As a result, the model focuses on a single objective, preventing global optimization of the relationships between PAN, LRMS, and HRMS.

To further overcome the limitations of phase-based training, we propose a framework that combines the strong supervision constraints of reduced-resolution images with the

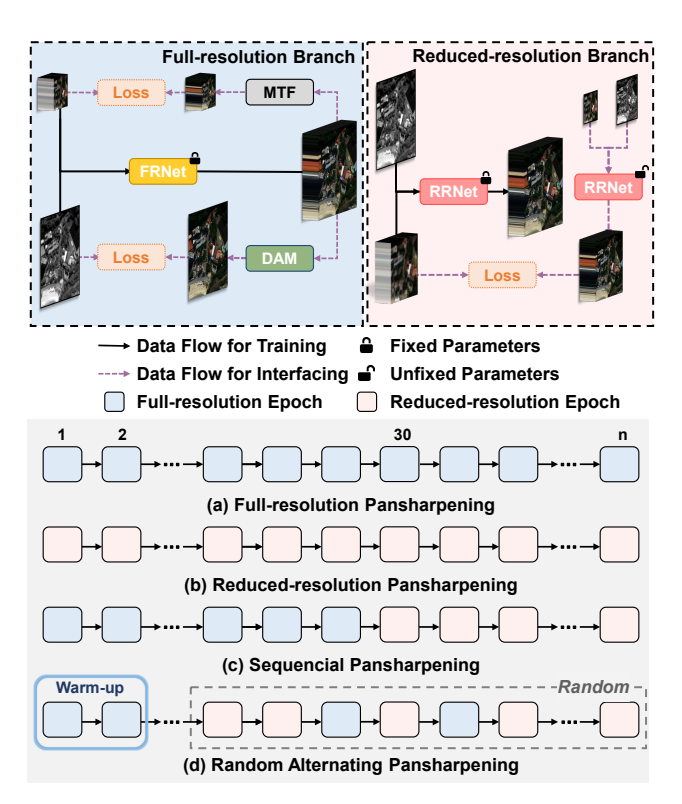


Figure 2. Pansharpening paradigms: (a) full-resolution training, (b) reduced-resolution training, (c) serial stage-wise training, (d) TRA-PAN with warm-up and random alternating training.

physical properties of full-resolution images. This framework uses a random alternating training strategy between resolutions, which helps regularize the model. By combining strong and weak supervision, it prevents overfitting to a single resolution and improves learning. We call this the Two-Stage Random Alternation Framework for Zero-Shot Pansharpening (TRA-PAN), as illustrated in Fig. 2 (d). It consists of two independent stages: the pre-training stage and the random alternating optimization (RAO) stage. Specifically, the pre-training stage includes the warm-up procedure and the Degradation-Aware Modeling (DAM) procedure. In the DAM procedure, we capture complex spatial relationships in real imaging systems. Through the warm-up procedure, the fusion model acquires excellent initial values from real data. The RAO stage then uses the previously obtained degradation model and the initial values of the fusion model to continue optimizing the fusion model.

In the DAM procedure, we employ a network to model the non-linear degradation process from HRMS to PAN images, capturing complex spatial relationships in real imaging systems. During the warm-up procedure, we train the fusion network only at full resolution to avoid distribution discrepancies from early reduced-resolution training that could harm the network. Later, reduced-resolution training is introduced to leverage its pixel-level supervision. In the RAO stage, a dynamic resolution strategy alternates between reduced- and

full-resolution training with a certain probability. Building on this stage, the RAO stage introduces a dynamic resolution training strategy, which alternates between reduced- and full-resolution training with a certain probability. This random alternating strategy regularizes the network, guiding it to explore better solutions by balancing strong supervision from reduced resolution with weaker supervision from full resolution. As a result, it improves the quality of HRMS generation and avoids the issues of resolution separation seen in traditional methods.

Although better fusion results are achieved with our twostage framework, DL-based methods still rely heavily on large-scale training data. Since our framework trains primarily at full resolution, it performs better in data-scarce conditions. This enables us to further leverage zero-shot methods, generating high-quality HRMS images with only a single LRMS/PAN pair. In conclusion, the contributions of this work are as follows:

- Our framework leverages both reduced- and full-resolution training, combining the strengths of each. The random alternating strategy boosts the network generalization by balancing strong and weak supervision from different resolutions. Additionally, the warm-up procedure accelerates the training process and mitigates the drawbacks of early reduced-resolution training, breaking away from the traditional approach of fine-tuning reduced-resolution images after full-resolution training.
- We implement zero-shot pansharpening, enabling highquality HRMS image generation from a single LRMS/PAN pair. This strategy offers significant advantages in datascarce scenarios, without requiring reference images or additional data.
- Our framework can be applied to various network backbones. Experiments show that it outperforms state-of-theart (SOTA) methods in both quantitative metrics and visual quality in real-world scenarios, demonstrating good practical application value.

## 2. Related Work

#### 2.1. Resolution-Utilization strategies

Recent research in pansharpening using DL-based methods can be categorized into three resolution-utilization strategies: reduced-resolution training, full-resolution training, and hybrid training. Reduced-resolution training, pioneered by Masi et al. [22], downscale LRMS and PAN images for network inputs, using the original LRMS as the supervision target. To further enhance the performance of this approach, several specific methods have been proposed. PNN [21] applies a simple three-layer fully-convolutional model. Fusion-Net [7] injects high-frequency details to improve both spatial and spectral quality. LAGNet [15] introduces LAGConv, a novel convolution operation that adapts kernels based on

local image context. This strategy, though effective, faces challenges due to distribution discrepancies.

Full-resolution training uses LRMS and PAN directly, enabling self-supervised learning, but requires careful design of loss functions. An early method in this category is the detail-preserving cross-scale learning strategy, which uses an MTF-GLP-HPM [38] model-based algorithm as a proxy for high-resolution ground truth. Another method, GTP-PNet [44], incorporates gradient transformation to improve both spatial and spectral accuracy. Pan-GAN [20], an unsupervised generative adversarial network framework, effectively preserves both spectral and spatial information by using two discriminators.

Hybrid training, combining both reduced and full-resolution strategies, attempts to maximize the strengths of both strategies. This strategy includes methods like Cross-Resolution Semi-Supervised Adversarial Learning, which improves consistency across resolutions through adversarial learning, and SUFNet [18], which integrates supervised and unsupervised networks for high-fidelity pansharpening. However, separating them into distinct stages may prevent fully leveraging the model's potential.

## 2.2. Zero-shot learning

Zero-shot learning has been explored in pansharpening, where the model is trained and tested on the same image, eliminating the need for extensive training data. Initially introduced by Shocher et al. [28] for image super-resolution, zero-shot learning relies on a lightweight network and crossscale patch matching, applying knowledge gained from one task to another. Nguyen et al. [24] extended this method to Sentinel-2 sharpening, using a CNN with symmetric skip connections that outperformed SOTA methods. Building on this, Wang et al. [37] proposed the Zero-Sharpen framework, combining deep learning and variational optimization to address scale-variance issues. Furthermore, Rui et al. [27] proposed a variational zero-shot method that uses a neural network to predict the coefficient tensor for HRMS-PAN relationships, optimizing both the coefficient and HRMS in a unified framework with DIP-type regularization and alternating minimization.

#### 3. Method

In this section, we first introduce the notation used in the following subsections and provide an overview of our method. The rest of the section is organized into two parts. The first part focuses on the pre-training stage, which covers both the DAM and warm-up procedures. The second part details the RAO stage.

#### 3.1. Notation

Here, we introduce some important notation. Let  $\mathcal{P} \in \mathbb{R}^{H \times W}$  represent the PAN image, where H and W de-

note height and width, respectively. The LRMS image,  $\mathcal{L} \in \mathbb{R}^{h \times w \times c}$ , has height h, width w and c spectral bands. The HRMS image,  $\mathcal{H} \in \mathbb{R}^{H \times W \times c}$ , is obtained by fusing the PAN and LRMS images. Additionally, the reduced resolution multispectral image (RRMS) is  $\mathcal{M}^L \in \mathbb{R}^{\frac{h}{r} \times \frac{w}{r} \times c}$ , and the reduced resolution panchromatic image (RRPAN) is  $\mathcal{M}^P \in \mathbb{R}^{\frac{H}{r} \times \frac{W}{r}}$ , where r is the resolution ratio between the LRMS and PAN images, i.e.  $r = \frac{H}{h}$  or  $r = \frac{W}{w}$ . Both of these downsampled images are obtained by using the MTF filter and the downsampling operation described in *supplementary material*. These processes are represented as follows:

$$\mathcal{M}^L, \mathcal{M}^P = \mathrm{MTF}_{\downarrow}(\mathcal{L}, \mathcal{P}) \tag{1}$$

where  $MTF_{\downarrow}(\cdot)$  represents the MTF filter and the downsampling operation.

#### 3.2. Overview

In this section, we will use the algorithm diagram Algorithm 1 to outline our TRA-PAN. Our method begins with the pre-training stage, consisting of the DAM and warmup procedures. They are represented by Line 1-Line 4 and Line 7-Line 12, respectively. In the DAM procedure, we need to train the spectral degradation-aware network with parameters  $\theta_D$ . During training, the network captures the spectral degradation between the LRMS image  $\mathcal{L}$  and the RRPAN image  $\mathcal{M}^P$ . This helps guide the fusion network's training in the following RAO stage. In the warm-up procedure, the fusion network is trained only at full-resolution. This helps accelerate network convergence, while also preventing the network from being overly influenced by the reduced-resolution training. This procedure provides a good initial value for the parameters  $\theta_R$ , laying the foundation for random alternating training. The method then proceeds to the RAO stage, which is represented by Line 5-Line 19. With the assistance of the DAM procedure, we optimize  $\theta_R$ by performing random alternating training on both reducedand full-resolution datasets. After optimization, we use the fusion network with  $\theta_R$  to perform the final inference, taking LRMS image  $\mathcal L$  and PAN image  $\mathcal P$  as inputs to generate HRMS image  $\mathcal{H}$ . We employ  $f_{\theta_R}(\cdot,\cdot)$  to represent the fusion network with learnable parameters.

$$\mathcal{H} = f_{\theta_{\mathcal{P}}}(\mathcal{L}, \mathcal{P}) \tag{2}$$

#### 3.3. Stage 1: Pre-training

**DAM Procedure** In this procedure, we address the challenge of learning the complex non-linear relationship between LRMS  $\mathcal L$  and RRPAN  $\mathcal M^P$ , and applying it to HRMS  $\mathcal H$  to generate PAN  $\mathcal D^P$ . Considering the data scarcity in zero-shot scenarios, complex network structures lead to overfitting and increase training time. To this end, we design a simple yet effective multi-layer perceptron (MLP) network.

During training, we first apply the tencrop method to  $\mathcal{L}$  and  $\mathcal{M}^P$ . Specifically, we crop the image into five parts at

```
Algorithm 1: Overall TRA-PAN Framework
   Data: LRMS \mathcal{L} and its ith augmentation \mathcal{L}_i. PAN \mathcal{P}
             and ith augmentation \mathcal{P}_i, DAM training
             epochs n_1, RAO training epochs n_2, Ratio p,
             Warm-up epochs m.
   Function: DAM procedure with parameters g_{\theta_D}(\cdot),
                   RAO fusion network with parameters
                   f_{\theta_R}(\cdot,\cdot), MTF and downsample function
                   MD(\cdot), Random function Rand(\cdot, \cdot, \cdot).
   Result: HRMS \mathcal{H}.
   // Training of DAM procedure
 1 for i = 1 to n_1 do
        \mathcal{D}_i^P \leftarrow g_{\theta_D}(\mathcal{L}_i)
         Update \theta_D based on Eq. (5)
 4 end
    // Training of RAO stage
 5 for j = 1 to n_2 do
         // Choose full or reduced with
               ratio p for full
         branch \leftarrow \text{Rand}(p, FULL, REDUCED)
         // Warm-up procedure
 7
        if j > m then
              \mathcal{M}_i^L \leftarrow MD(\mathcal{L}_i)
              \mathcal{M}_i^P \leftarrow MD(\mathcal{P}_i)
              \mathcal{M}_{i}^{H} \leftarrow f_{\theta_{R}}(\mathcal{M}_{i}^{L}, \mathcal{M}_{i}^{P})
Update \theta_{R} based on Eq. (6)
10
11
12
         end
        if branch is FULL then
13
              \widehat{\mathcal{H}} \leftarrow f_{\theta_R}(\mathcal{L}, \mathcal{P})
14
              \widehat{\mathcal{D}^P} \leftarrow g_{\theta_D}(\widehat{\mathcal{H}})
15
              \widehat{\mathcal{M}^L} \leftarrow MD(\widehat{\mathcal{H}})
16
              Update \theta_R based on Eq. (9)
17
18
        end
```

fixed positions and then perform horizontal flipping. This further prevents potential overfitting in the zero-shot scenario. This data augmentation process can be expressed as:

$$\mathcal{L}_i = \mathrm{DA}(\mathcal{L}), \mathcal{M}_i^P = \mathrm{DA}(\mathcal{M}^P) \tag{3}$$

where  $\mathrm{DA}(\cdot)$  denotes the data augmentation,  $\mathcal{L}_i$  and  $\mathcal{M}_i^P$  represent the ith augmented LRMS and RRPAN image, respectively. We then used the synthetic dataset to learn the degradation relationship from LRMS to RRPAN. The LRMS image  $\mathcal{L}_i$  is reshaped and processed by the MLP, which generates  $\widehat{\mathcal{D}_i^P} \in \mathbb{R}^{hw \times 1}$ . Then we perform reshaping operation again to obtain  $\mathcal{D}_i^P \in \mathbb{R}^{h \times w}$ . This procedure can be formally expressed as:

 $\mathcal{D}_i^P = g_{\theta_D}(\mathcal{L}_i) \tag{4}$ 

19 end

// Inference

20  $\mathcal{H} \leftarrow f_{\theta_R}(\mathcal{L}, \mathcal{P})$ 

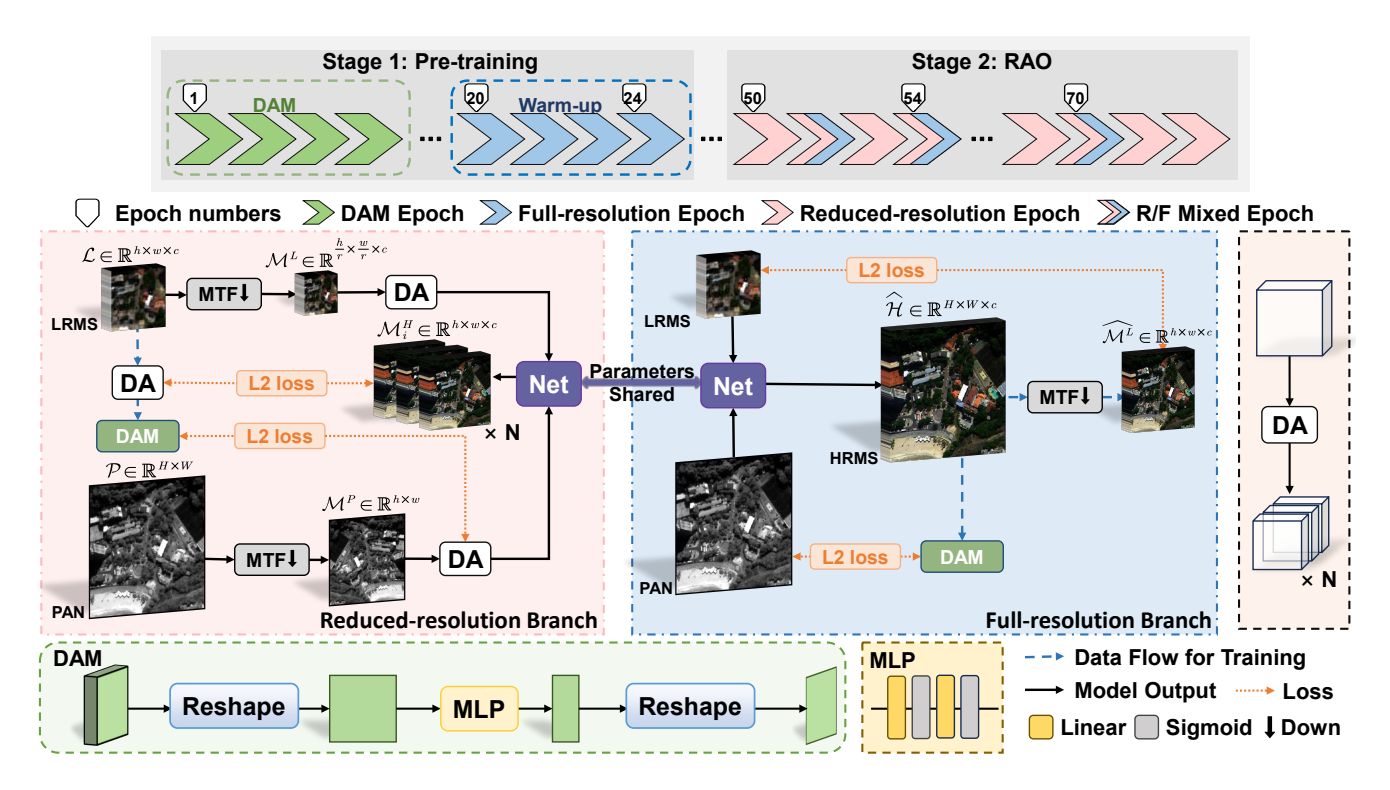


Figure 3. Flowchart of the TRA-PAN framework. The entire training process is illustrated by the progress bar at the top. First, the DAM procedure in the pre-training stage is initiated, and its network peremeters  $\theta_D$  proceeds to the RAO stage. After the DAM procedure is completed, the process moves to the warm-up procedure, which exclusively utilizes the full-resolution branch. Finally, the process enters the RAO stage, where random alternating training takes place. Note that the whole procedure only has one pair of LRMS and PAN images as input, then it could yield promising outcomes, especially for full-resolution data.

where  $g_{\theta_D}$  encompasses both the reshaping operations and the degradation network parameterized by  $\theta_D$ .

In order to learn this non-linear degradation relationship, we need to find the degradation network parameters  $\theta_D$ . The parameter update process for  $\theta_D$  is as follows:

$$\theta_D^* = \arg\min_{\theta_D} \|\mathcal{M}_i^P - \mathcal{D}_i^P\|_2^2 \tag{5}$$

where  $\theta_D^*$  is the updated  $\theta_D$ . Here, we use the  $\ell_2$  norm between the augmented ground-truth RRPAN image  $\mathcal{M}_i^P$  and the predicted degraded image  $\mathcal{D}_i^P$ , effectively guiding the network to restore spectral details lost during degradation.

Warm-up Procedure We begin learning  $\theta_R$  from the warm-up procedure, specifically by training the network in full-resolution only for m epochs. For details on how training is performed at full-resolution, refer to Sec. 3.4. This procedure aims to reduce the distribution gap between simulation images and real-world data, allowing the model to more effectively discover the general region of optimal solutions. Training initially at full-resolution contrasts with the traditional understanding, where networks are initially trained at reduced-resolution and then fine-tuned at full-resolution, leading to better performance. For further details on different warm-up epochs and strategies, refer to Sec. 4.4 and Sec. 4.3.

### 3.4. Stage 2: Random Alternating Optimization

**RAO Stage** The goal of the RAO stage is to train the network using a random alternating strategy, which takes advantage of pixel-level supervision and physical constraints. In each epoch, we always perform reduced-resolution training, and then we decide whether to perform full-resolution training, with probability p. This alternating strategy introduces randomness into the training process, acting as a regularization constraint to prevent overfitting to data at any single resolution. By ensuring that the network trains on the reduced-resolution dataset in every epoch, the strategy prevents the optimization direction from drifting due to continuous full-resolution training.

**Reduced-resolution** In the reduced-resolution training phase, we use the same data augmentation as in the DAM procedure to create a small dataset from a single  $\mathcal{M}^P/\mathcal{M}^L$  pair. The fusion model can be any pansharpening architecture, which is trained on this synthetic dataset. In our experiments, we adopt FusionNet as the base model. The output of this training phase is a fused image  $\mathcal{M}_i^H$ . The parameter  $\theta_R$  update process for the fusion network is as follows:

$$\theta_R^* = \arg\min_{\theta_R} \|\mathcal{M}_i^H - \mathcal{L}_i\|_2^2 \tag{6}$$

Table 1. Comparisons on WV3, QB, and GF2 full-resolution datasets, each with 20 samples. Best: <b>bold</b> , and second-best: <u>underline</u>	<u>2</u> .
--	------------

Methods	WV3		QB		GF2	
Methods	$\mathbf{D}_{\lambda}\downarrow\ \mathbf{D}_{s}\downarrow\ \mathbf{I}$	IQNR↑	$\mathbf{D}_{\lambda}\downarrow \mathbf{D}_{s}\downarrow \mathbf{D}_{s}$	HQNR↑	$\mathbf{D}_{\lambda}\downarrow\ \mathbf{D}_{s}\downarrow$	HQNR↑
MTF-GLP-FS [34]	0.020 0.063	0.918	0.047 0.150	0.810	0.035 0.143	0.828
BDSD-PC [31]	0.063 0.073	0.869	0.198 0.164	0.672	0.076 0.155	0.781
TV [25]	0.024 0.039	0.938	0.055 0.100	0.850	0.055 0.112	0.839
FusionNet [7]	0.025 0.044	0.932	0.057 0.052	0.894	0.035 0.101	0.867
LAGNet [15]	0.036 0.041	0.925	$0.086\ 0.068$	0.852	0.028 0.079	0.895
LGPNet [46]	0.022 0.039	0.940	0.074 0.061	0.870	0.030 0.080	0.892
CANNet [10]	$0.020 \ 0.029$	0.951	<b>0.038</b> 0.047	0.917	<b>0.019</b> 0.063	0.919
ZS-Pan [3]	0.026 0.031	0.945	0.053 0.082	0.870	0.054 0.100	0.852
PanMamba [14]	<u>0.020</u> 0.031	0.954	$0.049 \ \underline{0.044}$	0.910	$0.023 \ 0.057$	0.921
Proposed	0.019 0.015	0.966	<u>0.045</u> <b>0.033</b>	0.924	0.031 <b>0.040</b>	0.930

The objective is to minimize the  $\ell_2$  norm between  $\mathcal{M}_i^H$  and  $\mathcal{L}_i$ . This process updates the network parameters  $\theta_R$  to obtain the new parameters  $\theta_R^*$ . As a result, the network achieves improved performance in the reduced-resolution training phase, providing auxiliary support for the RAO stage.

**Full-resolution** During the full-resolution training phase, we leverage the model trained in the DAM procedure. Specifically, the predicted HRMS image  $\widehat{\mathcal{H}} \in \mathbb{R}^{H \times W \times c}$  is fed into the DAM-trained network to generate  $\widehat{\mathcal{D}^P} \in \mathbb{R}^{H \times W}$ . We then compute the spectral loss  $\mathcal{L}_{spectral}$  between  $\widehat{\mathcal{D}^P}$  and  $\mathcal{P}$ , which helps recover high-frequency details lost due to sensor MTF attenuation. This loss ensures the restoration of fine spectral details that are typically degraded during acquisition. The spectral loss is given by:

$$\mathcal{L}_{spectral} = \|\widehat{\mathcal{D}^P} - \mathcal{P}\|_2^2 \tag{7}$$

Additionally, the predicted HRMS image  $\widehat{\mathcal{H}}$  is downsampled using the MTF filters to obtain  $\widehat{\mathcal{M}^L} \in \mathbb{R}^{h \times w \times c}$ . To preserve spatial consistency, we introduce the spatial loss  $\mathcal{L}_{spatial}$ , which ensures the fusion process maintains the spatial details and structural integrity. The spatial loss is formulated as:

$$\mathcal{L}_{spatial} = \|\widehat{\mathcal{M}^L} - \mathcal{L}\|_2^2 \tag{8}$$

Throughout this process, we continue to optimize the parameter  $\theta_R$  used in the reduced-resolution phase. The optimization process in the RAO stage, which considers both spectral and spatial losses, is formalized as:

$$\theta_R^* = \arg\min_{\theta_R} (\lambda_1 \mathcal{L}_{spectral}(\widehat{\mathcal{D}^P}, \mathcal{P}) + \lambda_2 \mathcal{L}_{spatial}(\widehat{\mathcal{M}^L}, \mathcal{L}))$$
(9)

where  $\theta_R$  represents the parameters learned during the RAO stage, and  $\lambda_1$  and  $\lambda_2$  are hyper-parameters used to balance the importance of the spectral and spatial losses.

## 4. Experiments

In this section, we compare our TRA-PAN with the SOTA methods, conducting ablation studies and discussions on different warm-up strategies, training order and random sampling strategies. Finally, we discuss the number of warm-up

epochs m and sampling ratio p. Due to space limitations, the details on the sampling ratio can be found in the supplementary material.

#### 4.1. Datasets, Metrics and Training Details

In our experiments, we employ three datasets derived from satellite imagery captured by WorldView-3 (WV3), Quick-Bird (QB), and GaoFen-2 (GF2). During MTF filtering and downsampling, we use Wald's protocol [8, 36]. The datasets and associated data processing techniques are obtained from the PanCollection repository [9]. We use well-established evaluation metrics to assess our method. To evaluate the network performance in real-world scenarios, we use  $D_s$ ,  $D_{\lambda}$ and HQNR [2] as full-resolution evaluation metrics. Among them, HQNR is a comprehensive metric derived from  $D_s$ and  $D_{\lambda}$ , and it is effective in measuring the fusion quality of the image. Additionally, all loss functions in our model utilize the  $\ell_2$  loss, and the Adam optimizer[16] is employed at each stage. For the RAO stage, training is performed with the batch size of 8 over 250 epochs, while the DAM procedure is trained using the batch size of 1 over 250 epochs. All experiments are conducted on the NVIDIA GeForce RTX 4070 Ti SUPER GPU. If time is not a critical factor, the experiments can also be run on a desktop with only a CPU. More details can be found in the supplementary material.

#### 4.2. Comparison with SOTA methods

We evaluate our method against nine competitive approaches, including 1) three classical methods: MTF-GLP-FS [34], BDSD-PC [31], and TV [25]; 2) six DL-based methods FusionNet [7], LAGNet [15], LGPNet [46], CANNet [10], ZS-Pan [3] and PanMamba [14]. Among these deep learning methods, all except ZS-Pan are large-scale models trained on reduced-resolution simulated datasets. We choose to compare with these methods to showcase the generalization ability of our method, demonstrating that our method achieves better performance with fewer training time and parameters. The comparison with ZS-Pan is aimed at proving that our

https://github.com/liangjiandeng/PanCollection

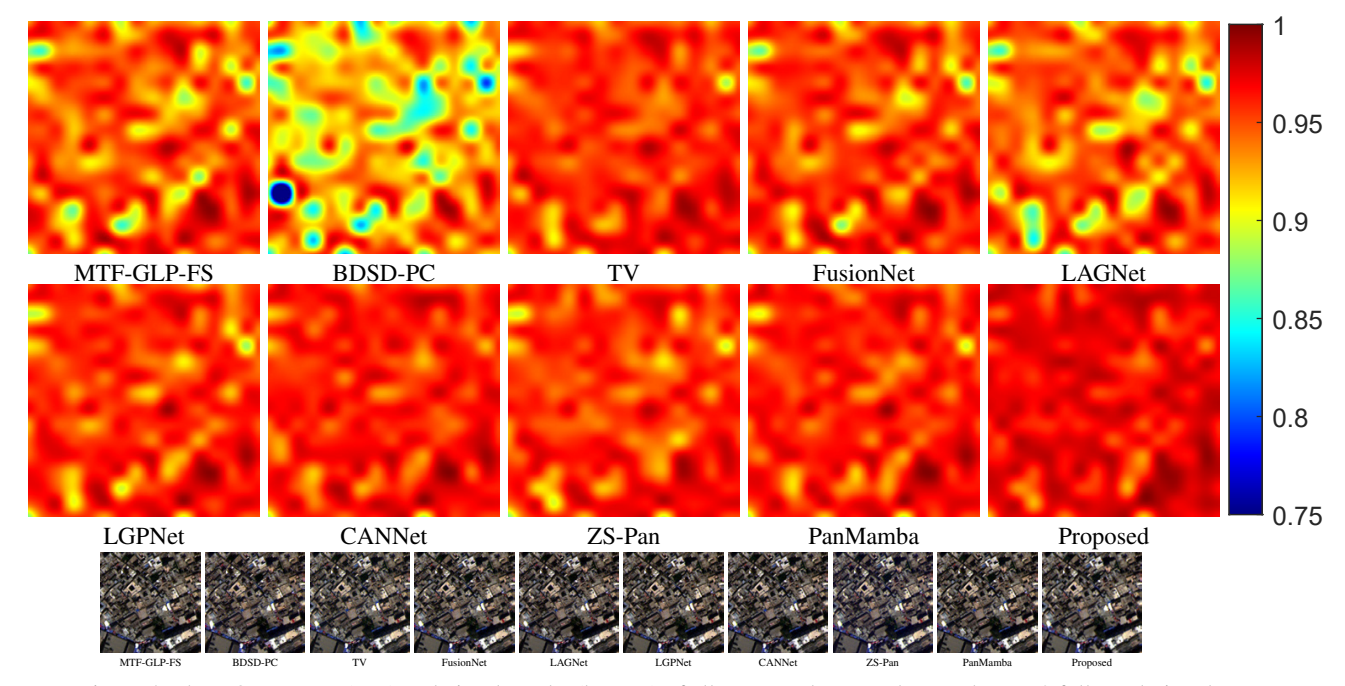


Figure 4. The HQNR maps (Top) and visual results (bottom) of all compared approaches on the WV3 full-resolution dataset.

method outperforms phase-based zero-shot methods in terms of generalization and performance.

To reduce training time and avoid potential overfitting, we use FusionNet as our fusion network. Since our proposed method is designed to demonstrate its capability in real-world scenarios, we primarily focus on comparisons at full resolution. Due to space limitations, the metrics and visual results at reduced resolution are presented in the *supplementary material*. Tab. 1 presents a comprehensive comparison of our method with state-of-the-art methods across three datasets. Notably, our method achieves high performance across all metrics, with particularly outstanding results in the WV3 dataset. Specifically, our method achieves a HQNR improvement of 0.012, 0.007, and 0.009 on the WV3, QB, and GF2 datasets, respectively, compared to the second-best results. These improvements highlight the clear advantages of our method, confirming its competitiveness in the field.

#### 4.3. Ablation Study and Analysis

Warm-up Strategy To demonstrate the effectiveness of the proposed warm-up strategy, we conducted an ablation experiment on the WV3 dataset, comparing three strategies: 20 epochs of warm-up at full-resolution, 20 epochs of warm-up at reduced-resolution and no warm-up. As shown in Tab. 2, the first row shows the strategy where warm-up is applied only to full-resolution training, emphasizing the key role full-resolution training plays in helping the network find optimal solutions. The second row shows the performance with warm-up applied at reduced-resolution, while the third row represents the scenario with no warm-up, entering the RAO stage directly. Our results indicate that, compared to

Table 2. Experiment on warm-up strategies at different resolutions.

Warmun Stratogy	WV3			
Warmup Strategy	$\mathbf{D}_{\lambda}\downarrow$	$\mathbf{D}s\!\!\downarrow$	<b>HQNR</b> ↑	
w Full	0.0193	0.0154	0.9657	
w Reduced	0.0286	0.0252	0.9469	
w/o Warmup	0.0266	0.0263	0.9478	

Table 3. Training order strategies for different resolutions.

Training Order	WV3			
Training Order	$\mathbf{D}_{\lambda}\downarrow  \mathbf{D}_{s}\downarrow$		HQNR↑	
Alternating	0.0193	0.0154	0.9657	
Full/Reduced	0.0316	0.0323	0.9372	
Reduced/Full	0.0234	0.0393	0.9384	

no warm-up, applying warm-up at reduced-resolution leads to a performance decrease, further confirming that reduced-resolution training serves only a supplementary role in the overall process. Overall, our experiments reveal that warm-up at full-resolution yields superior results, as training directly at reduced-resolution often causes the network to get stuck in suboptimal solutions, particularly when applied to real-world data.

**Training Order** We evaluate three different training order strategies to validate the effectiveness of our random alternating training. In the first row experiment, we apply a strategy where, for each epoch, the probability p of choosing full-resolution training is set to 0.8, and reduced-resolution training is selected with a probability of 0.2. In the second row experiment, we use the same number of full-resolution and reduced-resolution training epochs as in the first, but apply them in a fixed sequence: full-resolution training fol-

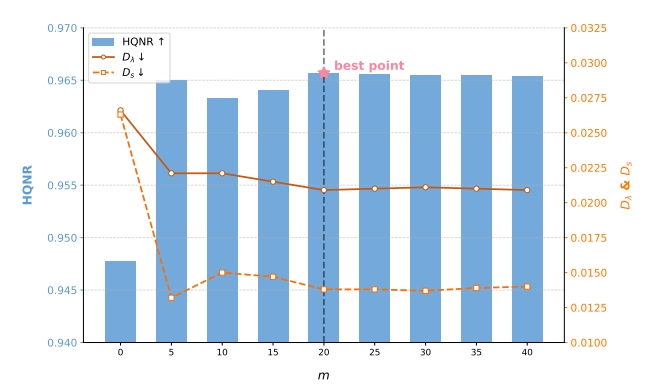


Figure 5. Effect of warm-up epochs on HQNR during full-resolution training.

lowed by reduced-resolution training, as represented by "Full/Reduced" in Tab. 3. In the third row experiment, the order is reversed, with reduced-resolution training first, followed by full-resolution training. The model's performance significantly decreases in the last two configurations, further supporting the effectiveness of the random alternating training strategy, as shown in Tab. 3.

Random Sampling Strategy In this part, we explore the impact of different random sampling strategies on the results. To evaluate this, we conducted three experiments with different configurations. In the first row experiment, we ensured reduced-resolution training for each epoch, with a certain probability p for selecting full-resolution training. The process for reduced-resolution training in each epoch is shown in Algorithm 1, specifically in Line 7-Line 12. In the second row experiment, we ensured full-resolution training for each epoch, with reduced-resolution training being selected with probability p. In this case, the contents of Line 7-Line 12 are swapped with Line 13-Line 18. In the third row experiment, after the warm-up procedure, we randomly select either reduced-resolution or full-resolution training for each epoch, which can be implemented by adding a sub-condition "branch is REDUCED" after Line 18.

The results show that continuous full-resolution training causes the model's optimization direction to drift due to weak supervision, as observed in the first and second-row experiments in Tab. 4. In our SOTA experiments, we used the strategy from the first-row experiment, which outperformed the other two strategies, further highlighting the negative impact of continuous full-resolution training on the model.

#### 4.4. Discussion

**Warm-up Epochs** This section explores the impact of the warm-up epoch number m on the results, a key variable in our method. All experiments are conducted on the WV3 dataset, with other hyper-parameters held constant. As shown in Fig. 5 and Fig. 6, as m increases from 0 to 20, the model's ability to identify the region of optimal solutions during full-resolution training improves, effectively reducing the

Table 4. Comparison of different random sampling strategies for training.

Dandam Campling Strategy	WV3			
Random Sampling Strategy	$\mathbf{D}_{\lambda}\downarrow$	$\mathbf{D}s\!\!\downarrow$	<b>HQNR</b> ↑	
Always Reduced	0.0193	0.0154	0.9657	
Always Full	0.0248	0.0326	0.9435	
Random	0.0256	0.0261	0.9491	

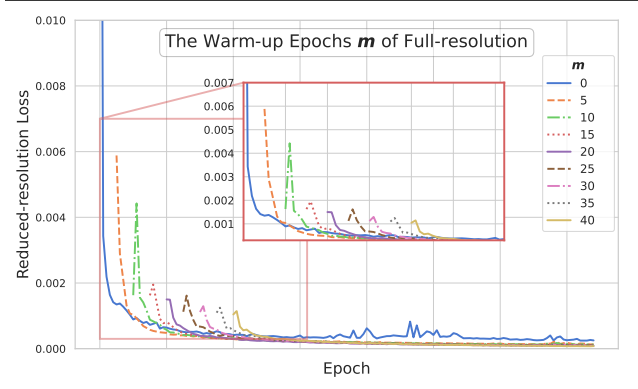


Figure 6. Warm-up epochs vs. the loss of fusion network during reduced-resolution training.

initial loss during reduced-resolution training, which significantly accelerates the networt's convergence, leading to an increase in HQNR. When m reaches 20, the model achieves the best initial value, facilitating optimal results in the subsequent RAO stage. However, when m becomes too large, the model may get trapped in a local optimum during full-resolution training, and the improvement in the initial loss during reduced-resolution training becomes less significant, limiting the corrective effect of reduced-resolution training and causing a slight drop in HQNR.

The line graph Fig. 6 shows the relationship between the number of warm-up epochs and the network loss during reduced-resolution training. This demonstrates that the number of warm-up epochs plays a critical role in determining final performance. Too few warm-up epochs prevent the model from reaching the optimal solution region, while too many warm-up epochs hinder its ability to adapt effectively to reduced-resolution, leading to suboptimal performance. Therefore, selecting an appropriate number of warm-up epochs is crucial to ensuring a strong starting point for the RAO stage.

## 5. Conclusion and Limitation

In this paper, we introduce TRA-PAN, a two-stage framework for zero-shot pansharpening that incorporates random alternating training and a warm-up procedure. The alternating training between reduced- and full-resolution images optimizes the fusion model, while the warm-up procedure accelerates convergence. Our experiments show that TRA-PAN outperforms state-of-the-art methods in both metrics and visual quality, particularly in data-scarce scenarios, prov-

ing its practical effectiveness. The limitation of our method lies in the slight increase in training time due to the random alternating between reduced- and full-resolution images, although it remains within an acceptable range.

#### References

- [1] Bruno Aiazzi, Luciano Alparone, Stefano Baronti, Andrea Garzelli, and Massimo Selva. Mtf-tailored multiscale fusion of high-resolution ms and pan imagery. *Photogrammetric Engineering & Remote Sensing*, 72(5):591–596, 2006.
- [2] Alberto Arienzo, Gemine Vivone, Andrea Garzelli, Luciano Alparone, and Jocelyn Chanussot. Full-resolution quality assessment of pansharpening: Theoretical and hands-on approaches. *IEEE Geoscience and Remote Sensing Magazine*, 10(3):168–201, 2022.
- [3] Qi Cao, Liang-Jian Deng, Wu Wang, Junming Hou, and Gemine Vivone. Zero-shot semi-supervised learning for pansharpening. *Information Fusion*, 101:102001, 2024.
- [4] Xiangyong Cao, Xueyang Fu, Danfeng Hong, Zongben Xu, and Deyu Meng. Pancsc-net: A model-driven deep unfolding method for pansharpening. *IEEE Transactions on Geoscience and Remote Sensing*, 60:1–13, 2021.
- [5] Jaewan Choi, Kiyun Yu, and Yongil Kim. A New Adaptive Component-Substitution-Based Satellite Image Fusion by Using Partial Replacement. *IEEE Transactions on Geoscience* and Remote Sensing, 49(1):295–309, 2011.
- [6] Matteo Ciotola, Sergio Vitale, Antonio Mazza, Giovanni Poggi, and Giuseppe Scarpa. Pansharpening by convolutional neural networks in the full resolution framework. *IEEE Transactions on Geoscience and Remote Sensing*, 60:1–17, 2022.
- [7] Liang-Jian Deng, Gemine Vivone, Cheng Jin, and Jocelyn Chanussot. Detail injection-based deep convolutional neural networks for pansharpening. *IEEE Transactions on Geo*science and Remote Sensing, page 6995–7010, 2021.
- [8] Liang-Jian Deng, Gemine Vivone, Cheng Jin, and Jocelyn Chanussot. Detail Injection-Based Deep Convolutional Neural Networks for Pansharpening. *IEEE Transactions on Geo*science and Remote Sensing, 59(8):6995–7010, 2021.
- [9] Liang-jian Deng, Gemine Vivone, Mercedes E. Paoletti, Giuseppe Scarpa, Jiang He, Yongjun Zhang, Jocelyn Chanussot, and Antonio Plaza. Machine Learning in Pansharpening: A benchmark, from shallow to deep networks. *IEEE Geo*science and Remote Sensing Magazine, 10(3):279–315, 2022.
- [10] Yule Duan, Xiao Wu, Haoyu Deng, and Liang-Jian Deng. Content-adaptive non-local convolution for remote sensing pansharpening. *IEEE/CVF Computer Vision and Pattern Recognition Conference (CVPR)*, 2024.
- [11] Xueyang Fu, Zihuang Lin, Yue Huang, and Xinghao Ding. A variational pan-sharpening with local gradient constraints. In 2019 IEEE/CVF Conference on Computer Vision and Pattern Recognition (CVPR), pages 10257–10266, 2019.
- [12] Xueyang Fu, Zihuang Lin, Yue Huang, and Xinghao Ding. A Variational Pan-Sharpening With Local Gradient Constraints. In 2019 IEEE/CVF Conference on Computer Vision and Pattern Recognition (CVPR), pages 10257–10266. IEEE, 2019.

- [13] Guiqing He, Siyuan Xing, Zhaoqiang Xia, Qingqing Huang, and Jianping Fan. Panchromatic and multi-spectral image fusion for new satellites based on multi-channel deep model. *Machine Vision and Applications*, 29:933–946, 2018.
- [14] Xuanhua He, Ke Cao, Jie Zhang, Keyu Yan, Yingying Wang, Rui Li, Chengjun Xie, Danfeng Hong, and Man Zhou. Panmamba: Effective pan-sharpening with state space model. *Information Fusion*, 115:102779, 2025.
- [15] Zi-Rong Jin, Tian-Jing Zhang, Tai-Xiang Jiang, Gemine Vivone, and Liang-Jian Deng. Lagconv: Local-context adaptive convolution kernels with global harmonic bias for pansharpening. In *Proceedings of the AAAI conference on artifi*cial intelligence, pages 1113–1121, 2022.
- [16] Diederik P. Kingma and Jimmy Ba. Adam: A method for stochastic optimization. In 3rd International Conference on Learning Representations, ICLR 2015, San Diego, CA, USA, May 7-9, 2015, Conference Track Proceedings, 2015.
- [17] Shutao Li, Haitao Yin, and Leyuan Fang. Remote sensing image fusion via sparse representations over learned dictionaries. *IEEE transactions on geoscience and remote sensing*, 51(9):4779–4789, 2013.
- [18] Qiang Liu, Xiangchao Meng, Feng Shao, and Shutao Li. Supervised-unsupervised combined deep convolutional neural networks for high-fidelity pansharpening. *Information Fusion*, 89:292–304, 2023.
- [19] Jiayi Ma, Han Xu, Junjun Jiang, Xiaoguang Mei, and Xiao-Ping Zhang. Ddcgan: A dual-discriminator conditional generative adversarial network for multi-resolution image fusion. *IEEE Transactions on Image Processing*, 29:4980–4995, 2020.
- [20] Jiayi Ma, Wei Yu, Chen Chen, Pengwei Liang, Xiaojie Guo, and Junjun Jiang. Pan-gan: An unsupervised pan-sharpening method for remote sensing image fusion. *Information Fusion*, 62:110–120, 2020.
- [21] Giuseppe Masi, Davide Cozzolino, Luisa Verdoliva, and Giuseppe Scarpa. Pansharpening by convolutional neural networks. *Remote Sensing*, 8(7):594, 2016.
- [22] Giuseppe Masi, Davide Cozzolino, Luisa Verdoliva, and Giuseppe Scarpa. Pansharpening by convolutional neural networks. *Remote Sensing*, 8(7):594, 2016.
- [23] Xiangchao Meng, Huanfeng Shen, Huifang Li, Liangpei Zhang, and Randi Fu. Review of the pansharpening methods for remote sensing images based on the idea of meta-analysis: Practical discussion and challenges. *Information Fusion*, 46: 102–113, 2019.
- [24] Han V Nguyen, Magnus O Ulfarsson, Johannes R Sveinsson, and Jakob Sigurdsson. Zero-shot sentinel-2 sharpening using a symmetric skipped connection convolutional neural network. In IGARSS 2020-2020 IEEE International Geoscience and Remote Sensing Symposium, pages 613–616. IEEE, 2020.
- [25] Frosti Palsson, Johannes R. Sveinsson, and Magnus O. Ulfarsson. A new pansharpening algorithm based on total variation. IEEE Geoscience and Remote Sensing Letters, page 318–322, 2013.
- [26] Xiangyu Rui, Xiangyong Cao, Zeyu Zhu, Zongsheng Yue, and Deyu Meng. Unsupervised pansharpening via low-rank diffusion model. *arXiv preprint arXiv:2305.10925*, 2(6), 2023.

- [27] Xiangyu Rui, Xiangyong Cao, Yining Li, and Deyu Meng. Variational zero-shot multispectral pansharpening. *IEEE Transactions on Geoscience and Remote Sensing*, 2024.
- [28] Assaf Shocher, Nadav Cohen, and Michal Irani. "zero-shot" super-resolution using deep internal learning. In *Proceedings of the IEEE conference on computer vision and pattern recognition*, pages 3118–3126, 2018.
- [29] Xin Tian, Yuerong Chen, Changcai Yang, and Jiayi Ma. Variational Pansharpening by Exploiting Cartoon-Texture Similarities. *IEEE Transactions on Geoscience and Remote Sensing*, 60:1–16, 2022.
- [30] Sergio Vitale and Giuseppe Scarpa. A detail-preserving cross-scale learning strategy for cnn-based pansharpening. *Remote Sensing*, 12(3):348, 2020.
- [31] Gemine Vivone. Robust band-dependent spatial-detail approaches for panchromatic sharpening. *IEEE Transactions on Geoscience and Remote Sensing*, page 6421–6433, 2019.
- [32] Gemine Vivone. Robust Band-Dependent Spatial-Detail Approaches for Panchromatic Sharpening. *IEEE Transactions on Geoscience and Remote Sensing*, 57(9):6421–6433, 2019.
- [33] Gemine Vivone, Rocco Restaino, Mauro Dalla Mura, Giorgio Licciardi, and Jocelyn Chanussot. Contrast and Error-Based Fusion Schemes for Multispectral Image Pansharpening. *IEEE Geoscience and Remote Sensing Letters*, 11(5): 930–934, 2014.
- [34] Gemine Vivone, Rocco Restaino, and Jocelyn Chanussot. Full scale regression-based injection coefficients for panchromatic sharpening. *IEEE Transactions on Image Processing*, 27(7): 3418–3431, 2018.
- [35] Gemine Vivone, Rocco Restaino, and Jocelyn Chanussot. Full Scale Regression-Based Injection Coefficients for Panchromatic Sharpening. *IEEE Transactions on Image Processing*, 27(7):3418–3431, 2018.
- [36] Lucien Wald, Thierry Ranchin, and Marc Mangolini. Fusion of satellite images of different spatial resolutions: Assessing the quality of resulting images. *Photogrammetric engineering and remote sensing*, 63(6):691–699, 1997.
- [37] Hebaixu Wang, Hao Zhang, Xin Tian, and Jiayi Ma. Zero-sharpen: A universal pansharpening method across satellites for reducing scale-variance gap via zero-shot variation. *Infor-mation Fusion*, 101:102003, 2024.
- [38] Peng Wang, Hongyu Yao, Cai Li, Gong Zhang, and Henry Leung. Multiresolution analysis based on dual-scale regression for pansharpening. *IEEE Transactions on Geoscience and Remote Sensing*, 60:1–19, 2021.
- [39] Wenqing Wang, Licheng Jiao, and Shuyuan Yang. Fusion of multispectral and panchromatic images via sparse representation and local autoregressive model. *Information fusion*, 20: 73–87, 2014.
- [40] Han Xu, Jiayi Ma, Junjun Jiang, Xiaojie Guo, and Haibin Ling. U2fusion: A unified unsupervised image fusion network. *IEEE transactions on pattern analysis and machine* intelligence, 44(1):502–518, 2020.
- [41] Gang Yang, Xiangyong Cao, Wenzhe Xiao, Man Zhou, Aiping Liu, Xun Chen, and Deyu Meng. Panflownet: A flow-based deep network for pan-sharpening. In *Proceedings of the IEEE/CVF International Conference on Computer Vision*, pages 16857–16867, 2023.

- [42] Guishuo Yang, Kai Zhang, Feng Zhang, Jian Wang, and Jiande Sun. Cross-resolution semi-supervised adversarial learning for pansharpening. *IEEE Transactions on Geoscience and Remote Sensing*, 61:1–17, 2023.
- [43] Yong Yang, Mengzhen Li, Shuying Huang, Hangyuan Lu, Wei Tu, and Weiguo Wan. Multi-scale spatial-spectral attention guided fusion network for pansharpening. In *Proceedings of the 31st ACM International Conference on Multimedia*, pages 3346–3354, 2023.
- [44] Hao Zhang and Jiayi Ma. Gtp-pnet: A residual learning network based on gradient transformation prior for pansharpening. ISPRS Journal of Photogrammetry and Remote Sensing, 172:223–239, 2021.
- [45] Wenwen Zhang, Jing Li, Feng Zhang, Jiande Sun, and Kai Zhang. Unsupervised change detection of multispectral images based on pca and low-rank prior. *IEEE Geoscience and Remote Sensing Letters*, 19:1–5, 2021.
- [46] Chen-Yu Zhao, TianJing Zhang, Ran Ran, Zhi-Xuan Chen, and Liang-Jian Deng. Lgpconv: Learnable gaussian perturbation convolution for lightweight pansharpening. *International Joint Conference on Artificial Intelligence (IJCAI)*, 2023.

## A. Complexity Analysis of MLP Architecture

Our MLP design consists of 3 layers, with a hidden layer size of 32 and the Sigmoid activation function. This simple architecture is intentionally chosen to prevent overfitting, especially in data-scarce zero-shot scenarios. Despite its simplicity, the MLP effectively captures the required degradation relationships, and the experimental results demonstrate its excellent performance.

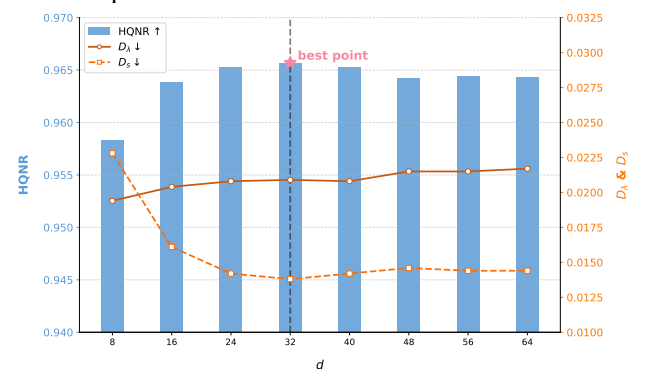


Figure 7. Effect of hidden layer size d on HQNR during training.

In this study, we conducted a systematic experiment on the architectural selection of Multilayer Perceptron (MLP) networks, providing quantitative support for the rational design of MLP structures. We focused on investigating the impact of hidden layer size d on model complexity and performance. The experiments were conducted on the WV3 dataset, ensuring strict control of variables by keeping other hyperparameters constant. A line plot illustrates the training performance trends across different representative values of d as a function of training epochs. The results indicate that when the hidden layer size is small, the network's expressiveness is limited, leading to insufficient modeling capability of the DAM degradation process and ultimately poor performance. As dd increases to the optimal value of 32, the network achieves a balance between fitting capacity and generalization ability, significantly enhancing the simulation performance. However, beyond this optimal scale, further increases in model complexity lead to overfitting, degrading generalization ability and ultimately deteriorating training performance.

#### **B.** Explanation of MTF-matched filters

The MTF [1, 33] matching filter is used to downsample PAN, LRMS, and HRMS images. The MTF is primarily employed to design a low-pass filter that matches the actual response of the MS sensor, thereby more realistically simulating the low-frequency information captured by the sensor during the downsampling process. The image degradation process can be expressed as follows:

$$Y = (X \otimes K) \downarrow_r + n_1 \tag{10}$$

In this equation, the symbol ⊗ denotes the convolution operation, which is used to apply the blur kernel K. The blur kernel  $K \in \mathbb{R}^{k \times k}$  is a preset filter whose parameters, such as the standard deviation  $\sigma$ , are determined based on the sensor's gain at the Nyquist frequency to match the actual MTF of the sensor. The operator  $\downarrow_r$  indicates down-sampling by a factor of r. Additionally,  $n_1$  represents a small residual value, typically modeled by a zero-mean Gaussian distribution, which accounts for noise during the degradation process. This filter typically has a Gaussian-like shape, and its sole free parameter, the standard deviation, is set according to the sensor's gain at the Nyquist frequency, allowing it to closely match the MS sensor's MTF. By employing this filter in our network, we are able to more accurately simulate the sensor characteristics associated with resolution degradation when changing data scales.

## C. Details of Data Augmentation

During the DAM and RAO stages of the reduced-resolution training, we applied data augmentation techniques. Specifically, we employed the Tencrop method, which extracts five fixed-position crops from the image. These five crops correspond to the top-left corner, top-right corner, bottom-left corner, bottom-right corner, and the center region of the image. Then, each of these five cropped regions is subjected to horizontal flipping, resulting in a dataset composed of 10 cropped images. In the zero-shot scenario, data augmentation further helps prevent the potential overfitting of the model.

## D. Analysis of Sampling Ratio

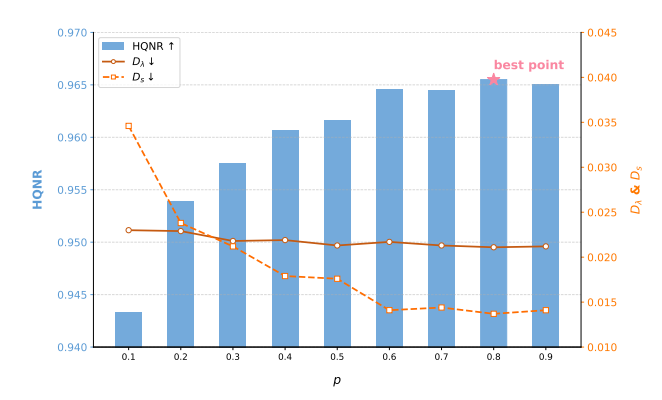


Figure 8. Effect of random sampling ratio p on HQNR during training.

Similar to the warmup epoch number m, the random sampling ratio p is another critical variable in our approach, indicating the probability of inserting full-resolution training in each epoch. Likewise, we performed experiments on the WV3 dataset, maintaining all other hyperparameters constant. As illustrated in Fig. 8, as the ratio p increases from 0.1 to 0.8, the model becomes more effective in combining

the strengths of both full-resolution and reduced-resolution training. When p reaches 0.8, the best balance is achieved, resulting in optimal performance. However, as p increases further, the model is subjected to insufficient pixel-level supervision, which affects its ability to preserve spatial information, resulting in a slow decline in HQNR.

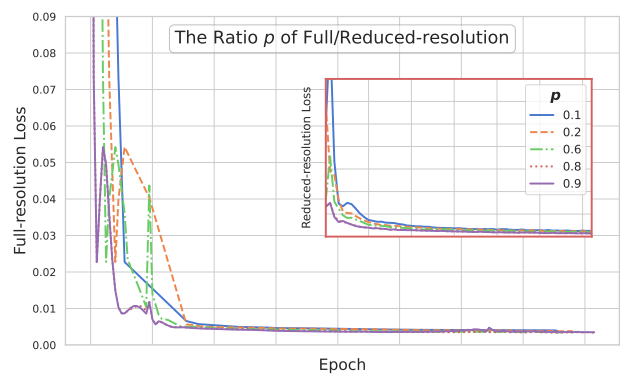


Figure 9. Effect of the ratio p on the loss of the fusion network during Full/Reduced-resolution training.

This study further explores the role of the random sampling ratio p in both full-resolution and downsampledresolution training, analyzing its impact on the model optimization process through loss curve evaluations. Experimental results indicate that when training with full resolution, an excessively small p = 0.1 prevents the model from fully leveraging high-resolution information, leading to an over-reliance on downsampled features. Consequently, the training process is prone to local optima, resulting in a slow decline in loss. Even a slight increase in p = 0.2fails to effectively mitigate this issue and instead introduces instability in loss reduction. d When p is increased to 0.8, the dominant role of full-resolution features is effectively balanced with the auxiliary benefits of downsampled information, leading to a more efficient and stable training process that achieves optimal performance. Furthermore, a comparison with p = 0.6 reveals that at p = 0.8, the model exhibits greater robustness to the introduction of downsampled features after the warmup phase, further optimizing the convergence trajectory. However, when p is further increased to 0.9, the supplementary benefits of downsampled information diminish, leading to increased fluctuations in the later stages of training, ultimately compromising the convergence quality.

## E. Details on Experiments and Discussion

#### E.1. Datasets

We conducted experiments on data collected from the WorldView-3 (WV3), QuickBird (QB), and GaoFen-2 (GF2) satellites. The datasets consist of images cropped from entire remote sensing images, divided into training and testing sets. The training set comprises PAN/LRMS/GT image pairs

Table 5. Experiment of different backbones in WV3 dataset.

Backbone	WV3			
Dackbolle	$\mathbf{D}_{\lambda}\downarrow  \mathbf{D}s\downarrow$		<b>HQNR</b> ↑	
TRA-PAN	0.0193	0.0154	0.9657	
LAG	0.0939	0.1065	0.8103	
LGP	0.0710	0.1408	0.7988	

obtained by downsampling simulation, with dimensions of  $64\times64$ ,  $16\times16\times C$  and  $64\times64\times C$ , respectively. The WV3 training set contains approximately 10,000 pairs of eight-channel images (C=8), while the QB training set contains around 17,000 pairs of four-channel images (C=4). GF2 training set has about 20,000 pairs of four-channel images (C=4). The reduced-resolution testing set for each satellite consists of 20 downsampling simulated PAN/LRMS/GT image pairs with various representative land covers, with dimensions of  $256\times256$ ,  $64\times64\times C$ , and  $256\times256\times C$ , respectively. The full-resolution test set includes 20 pairs of original PAN/LRMS images with dimensions of  $512\times512$  and  $128\times128$ . Our datasets and data processing methods are downloaded from the PanCollection repository [9].

### E.2. Training Details

For training TRA-PAN on the WV3 dataset, we employed the  $\ell_2$  loss function and the Adam optimizer [16] during training. We chose a ratio of 0.8 for the RAO phase of training. In full-resolution training, the initial learning rate was set to 0.0005 and was reduced to the order of  $10^{-3}$  after 250 epochs. For downsampled training, the initial learning rate remained at 0.0005 but was decreased to the order of  $10^{-4}$ after 400 epochs. The total training duration for both settings was 250 epochs. During the DAM stage, the learning rate was set to 0.0005. Regarding the network architecture, the number of channels in the hidden layers was configured to 32. For the QB dataset, we adjusted the warm-up period to five iterations and modified the ratio to 0.7, while keeping all other parameters identical to those used for the WV3 dataset. For the GF2 dataset, the warm-up period was extended to 80 iterations, with all other parameters remaining consistent with those used for the WV3 dataset.

## E.3. Replacing Fusion Network Backbone

In this section, we replaced the fusion network used in the RAO stage with LAGNet, LGPNet, and FusionNet as the backbone of our network. From Tab. 5, we found that using LAGNet and LGPNet significantly degraded the fusion results. This is because in a zero-shot scenario, complex networks are more prone to overfitting.

#### E.4. Additional Results

In the following figures, we present a comparison of the visualisation outputs of the various methods on sample images from the WV3, QB, and GF2 datasets, including the residuals between the outputs at full resolution versus the HQNR images, the outputs of the reduced resolution samples and the ground truth.

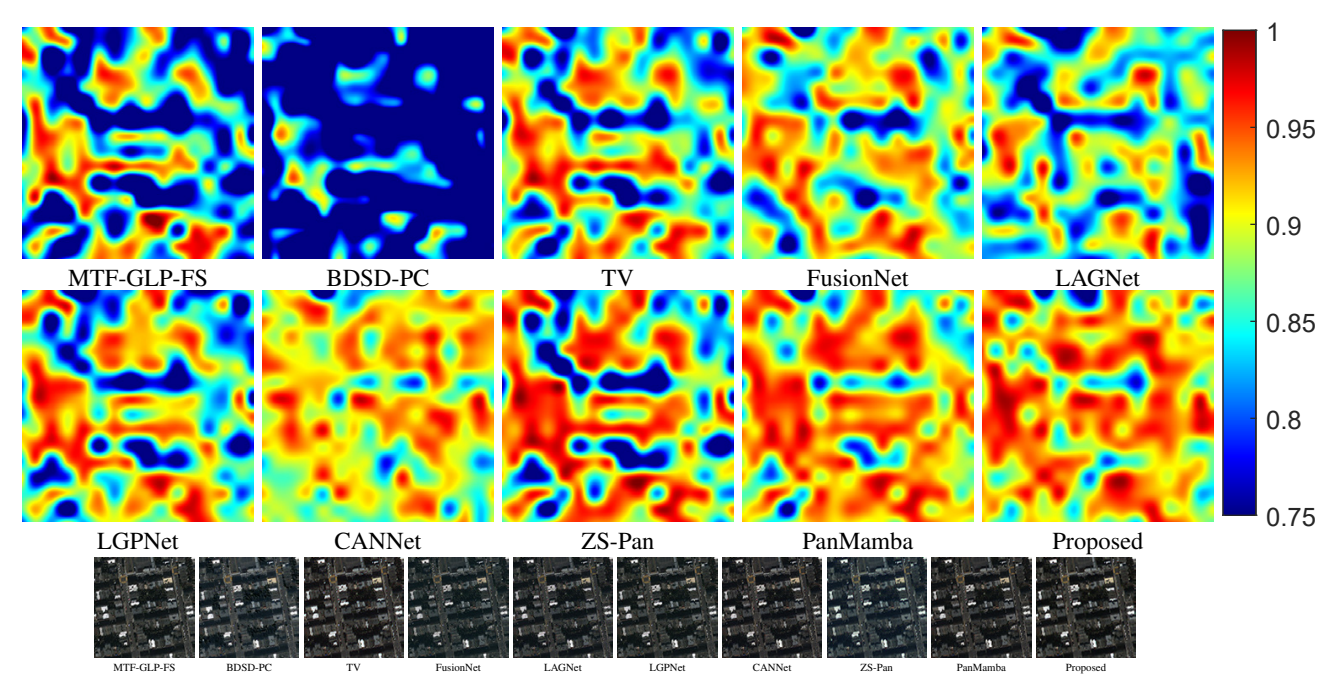


Figure 10. The HQNR maps (Top) and visual results (bottom) of all compared approaches on the QB full-resolution dataset.

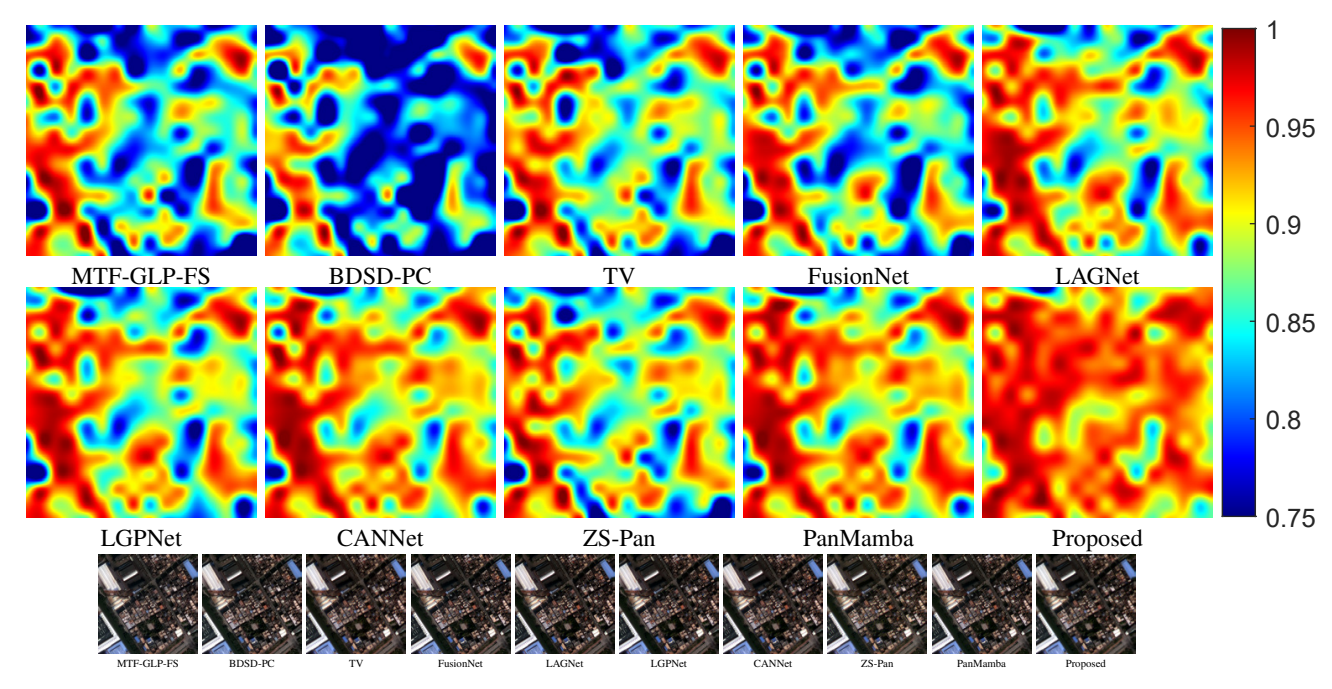


Figure 11. The HQNR maps (Top) and visual results (bottom) of all compared approaches on the GF2 full-resolution dataset.

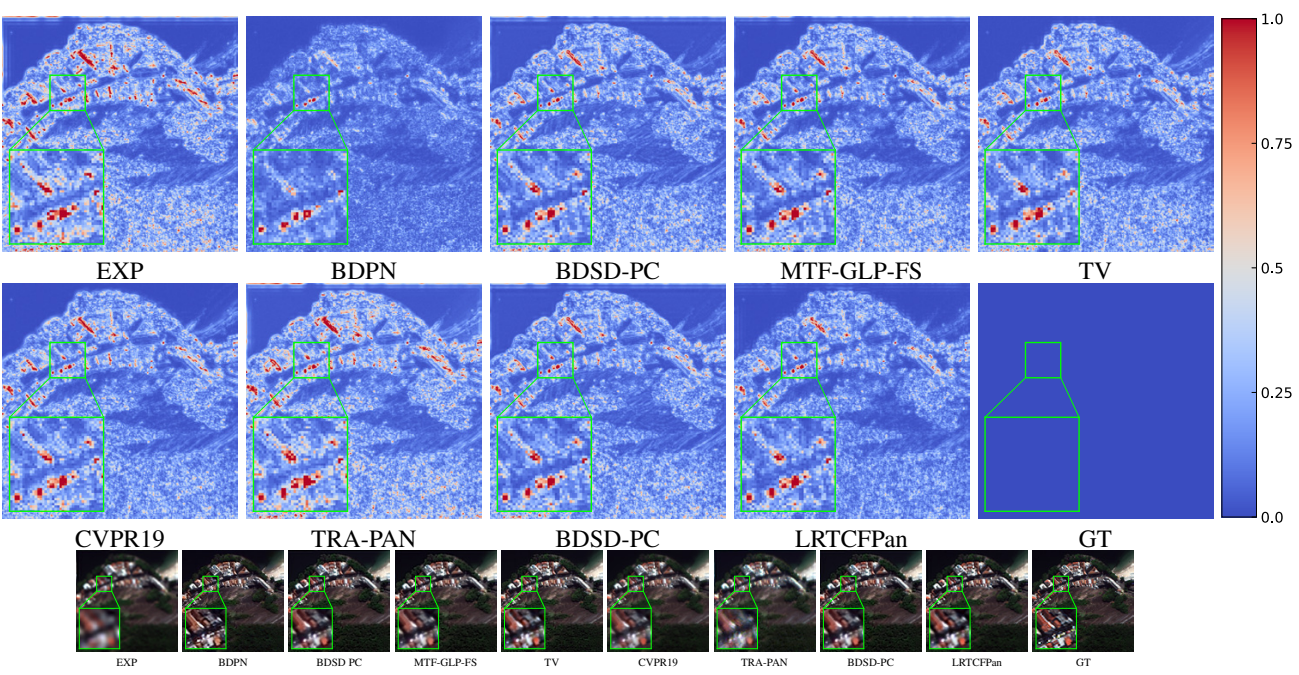


Figure 12. Qualitative result comparison between benchmarked methods on the sample image from WV3 reduced-resolution dataset. The first row presents the residual compared to the ground truth, while the second row shows RGB outputs.

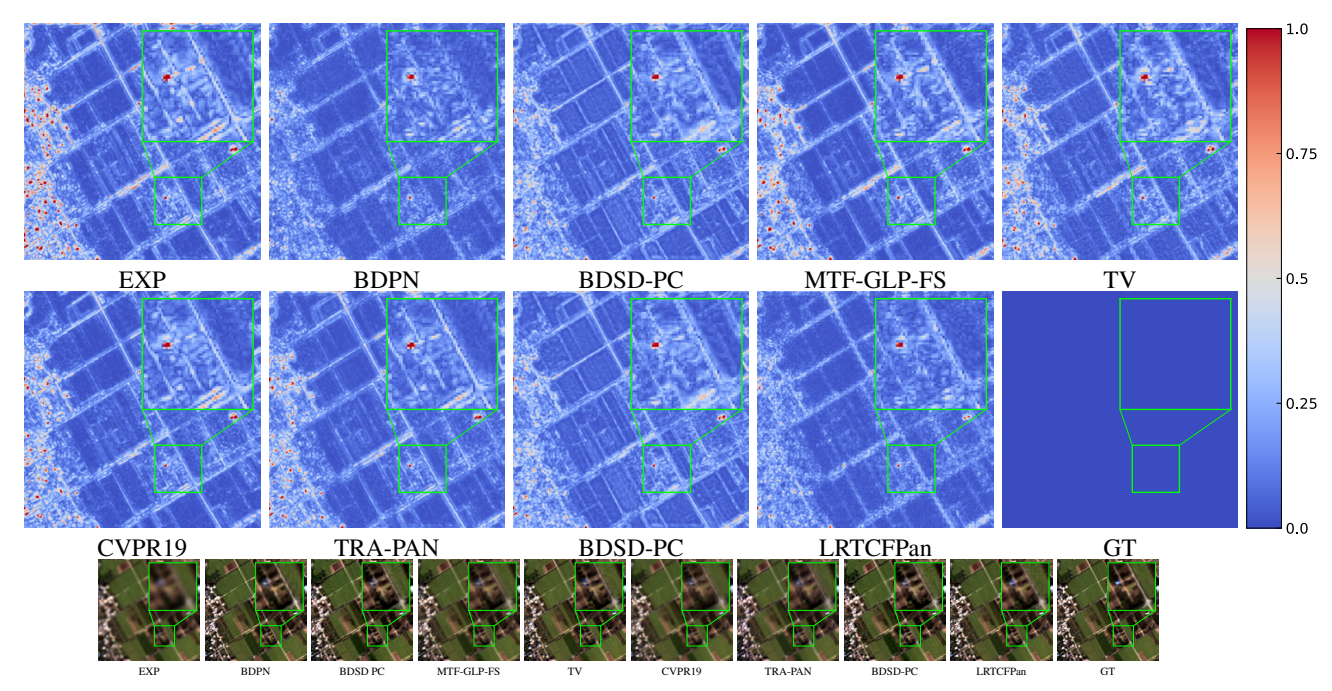


Figure 13. Qualitative result comparison between benchmarked methods on the sample image from GF2 reduced-resolution dataset. The first row presents the residual compared to the ground truth, while the second row shows RGB outputs.

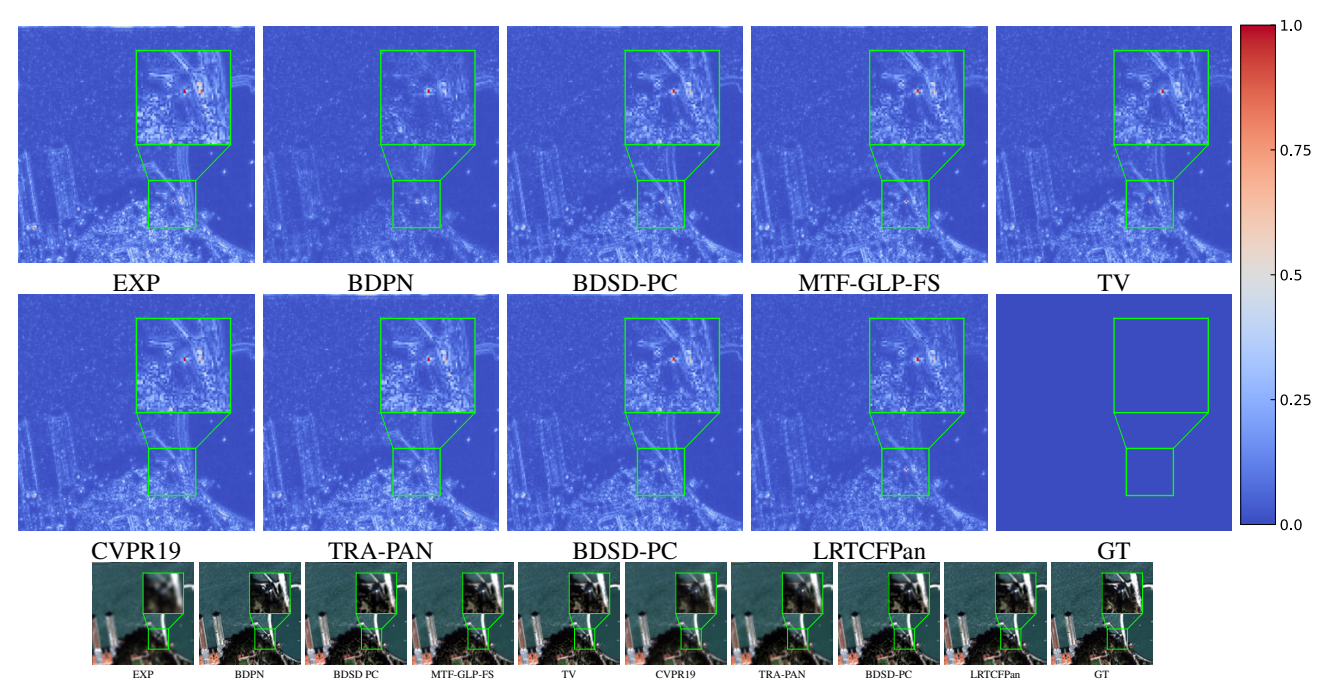


Figure 14. Qualitative result comparison between benchmarked methods on the sample image from QB reduced-resolution dataset. The first row presents the residual compared to the ground truth, while the second row shows RGB outputs.